

SHIMMER: A Spatial Heterodyne Spectrometer for Remote Sensing of Earth's Middle Atmosphere

John M. Harlander *Department of Physics, Astronomy and Engineering Science, St. Cloud State University, St. Cloud, Minnesota*

Fred L. Roesler, *Department of Physics, University of Wisconsin-Madison, Madison, Wisconsin*

Joel G. Cardon, Christoph R. Englert and Robert R. Conway *The US Naval Research Laboratory, Code 7641, Washington, D.C.*

© 2001 Optical Society of America, Inc., OCIS Codes: 010.1290, 120.3180, 120.6200

Abstract

It is well known and demonstrated that interference spectroscopy offers capabilities for obtaining passive remote optical sensing spectra of high precision while achieving economies in size, cost, and ease of deployment compared to more conventional systems. In this paper we describe the development of a near-ultraviolet Spatial Heterodyne Spectrometer (SHS) designed for remote sensing of the global distribution of the hydroxyl radical OH in the earth's middle atmosphere. The instrument, known as SHIMMER (Spatial Heterodyne Imager for Mesospheric Radicals), is expected to obtain its first OH measurement from space in early 2002 from the Space Shuttle.

1. Introduction

The instrument described in this paper draws its primary scientific motivation from the Middle Atmosphere High Resolution Spectrograph Investigation (MAHRSI), which was designed specifically to make global measurements of OH in the middle atmosphere from low-Earth orbit. The importance of the hydroxyl radical OH in the photochemistry of planetary atmospheres has been recognized for more than 50 years¹; nevertheless, recent satellite observation using high resolution ultraviolet spectroscopy have resulted in a number of unexpected results. The MAHRSI measurements provide

firm evidence that the photochemistry of ozone and the odd-hydrogen HO_x family (H , OH and HO_2) as formulated in current atmospheric models cannot consistently explain the abundance of OH throughout the middle atmosphere²⁻⁴. In addition, comparisons of the MAHRSI data with direct measurements of mesospheric H_2O by the Halogen Occultation Experiment (HALOE) instrument on the Upper Atmospheric Research Satellite (UARS) satellite have revealed that the OH data also comprise a powerful measure of the distribution of mesospheric water vapor². A layer of H_2O detected near an altitude of 65 km violates our understanding of the processes by which water is produced in and transported through the middle atmosphere. MAHRSI data also lead to the discovery of a water vapor layer near the Arctic summer mesopause, possibly related to the formation of high altitude (82km) Polar Mesospheric Clouds (PMCs); it has been suggested⁵ that the increasing occurrence of such clouds is a vivid indication of atmospheric change caused by human activity. There is, however, very little quantitative knowledge of why PMCs form and why they vary.

In its measurement of OH , MAHRSI observed the ultraviolet (UV) solar resonant fluorescent band of OH near 308 nm wavelength with a resolving power of about 15,000⁶, which was high enough to separate unambiguously the OH emission from the bright spectrally complex background formed by sunlight Rayleigh scattered by the ambient atmosphere. The MAHRSI results and the atmospheric science questions they raise clearly define the need and the requirements for a high spectral resolution UV instrument with high spatial resolution and high throughput. However, the weight (138 kg), size (120 cm X 85 cm X 23 cm), complexity and responsivity of a conventional spectrograph like MAHRSI make it unsuitable for future satellite mission opportunities.

Using an innovative optical technique called SHS for Spatial Heterodyne Spectroscopy⁷⁻⁸, we have developed an instrument called the Spatial Heterodyne Imager for Mesospheric Radicals, or SHIMMER, which appears capable of out-performing

MAHRSI in a much smaller and lighter package. Extensive laboratory testing indicates that the performance of SHIMMER is near theoretical predictions. Despite its small size and great simplicity, laboratory calibrations demonstrate that the responsivity of SHIMMER $[(\text{counts/sec})/(\text{kRayleigh/nm})]$ is more than 10,000 times larger than MAHRSI while its spectral resolution (0.0058 nm) is 3.5 times better. Its mechanical volume and mass are approximately 17% of MAHRSI's. A proof-of-concept test flight of SHIMMER is planned from the middeck of the Space Shuttle using the high-quality optical window in the orbiter side hatch. Environmental tests have verified that the design is suitable for Shuttle launch environments.

The following sections describe the fundamental concepts, design, laboratory evaluation, history and current status of SHIMMER.

2. Properties of SHS instruments

Spatial heterodyne spectroscopy is particularly well suited to UV applications that require high resolving power and high throughput over a relatively narrow spectral band. In general, however, an SHS can be tuned to work in any spectral region with control over the tradeoff between spectral resolution and bandwidth. SHS is similar to Fourier transform spectroscopy (FTS), with three primary differences. First, SHS effectively heterodynes the interferogram about a selected reference wavelength, resulting in easily measurable low spatial frequency fringes produced by wavelengths in the passband of the instrument. Second, the SHS has no moving parts, even in the field-widened mode, and therefore is much smaller, lighter, and less complex mechanically than FTS instruments making similar measurements. Third, SHS uses an imaging detector to record a fringe pattern localized inside the interferometer, consequently phase errors resulting from optical defects can be easily corrected in the data reduction. Compared

with more conventional grating spectrometers such as MAHRSI, SHS achieves orders of magnitude higher throughput at similar or higher spectral resolution in a much smaller package⁸. As is the case with FTS instruments, zero, one, or two dimensions of spatial information can be obtained by appropriate choice of the optics prior to the interferometer.

2.1 Basic SHS: on-axis analysis

The basic SHS concept is depicted in the Figure 1, where the image of an extended scene is collimated to form a beam incident on the beamsplitter. Diffraction gratings in each arm return the light to the beam splitter. Lenses L_2 and L_3 in the exit beam image the gratings onto a position sensitive detector. The gratings are positioned so that they are the same distance from the beamsplitter along the optical axis and are set at an angle θ_L such that rays of a certain wavelength incident on the gratings parallel to the optical axis retroreflect, returning parallel to the optical axis. At this wavelength, called the Littrow wavelength the recombining wavefronts exit the interferometer completely in phase with each other combining constructively at all points across the aperture. For a wavelength slightly different from the Littrow wavelength, the diffracted beams return at a small angle to the optical axis, and the recombining wavefronts are crossed as depicted in the figure. In this case the phase difference between the two wavefronts changes from a maximum at one edge, to zero in the middle, and back to maximum at the other edge, resulting in a Fizeau fringe pattern whose spatial frequency is related to the angle at which the wavefronts cross.

The off-Littrow angle γ , at which incident light parallel to the optical axis of wave-number σ exits the interferometer is given by the grating equation,

$$s [\sin \mathbf{q}_L + \sin (\mathbf{q}_L - \mathbf{g})] = m/d \quad (1)$$

where m is the order of diffraction, θ_L is the Littrow angle and $1/d$ is the grating groove density. The spatial frequency of Fizeau fringes is related to the wavenumber of light by the equation,

$$f_x = 2s \sin g \approx 4(s - s_0) \tan q_L \quad (2)$$

where the approximation assumes small γ , and s_0 is the Littrow wavenumber for which $\gamma = 0$. For axial rays, the intensity at the fringe localization plane for incident spectral density $B(\sigma)$ is given by

$$I(x) = \int_0^\infty B(s) \{1 + \cos[2p(4(s - s_0)x \tan(q_L))]\} ds \quad (3)$$

where x is measured in the dispersion plane of the gratings. Note that, except for the constant term, $I(x)$ is the Fourier transform of the input spectrum. The fringe localization plane is at the gratings, and therefore the gratings are imaged directly on the detector to produce an interferogram that is then Fourier transformed to recover the input spectrum. The maximum achievable resolving power is given by $R_0 = 4Ws \sin q_L$ where W is the width of the gratings. It can be shown that R_0 is simply equal to the total number of grating grooves imaged onto the detector.

The non-aliased passband of the SHS is limited by the number of samples across the interferogram. If the detector has N pixels in the dispersion plane of the gratings (the plane of figure 1), $N/2$ non-aliased spectral resolution elements can be measured, resulting in a passband of $Ns/(2R)$. In order to achieve this maximum bandwidth, the optics that image the gratings on the detector must adequately reproduce $N/2$ fringes at the detector.

The symmetry of the cosine interferogram in Equation 3 results in an ambiguity between wavenumbers above and below the Littrow wavenumber ($\sigma \pm \Delta\sigma$) as their fringe frequencies are identical. This has the effect of folding the spectrum about the

Littrow wavenumber. This ambiguity can be handled in one of three ways: 1) The cosine symmetry can be broken by introducing a small tilt to one of the gratings to produce low spatial frequency fringes in the y-dimension of the detector in addition to the wavenumber-dependent fringes in the x direction illustrated in Equation 3. With this y-tilt the resulting fringe patterns are rotated clockwise or counter clockwise depending upon whether σ is above or below the Littrow wavenumber. A two-dimensional Fourier transform distinguishes between these fringe patterns. 2) A prefilter can be used to block light on one side of Littrow or 3) The folded spectrum can be accounted for in the spectral analysis. The prefilter solution to this problem was chosen for SHIMMER.

2.2 Off Axis Analysis

By including off-axis angles in the grating equation, it can be shown⁷ that the solid angle field-of-view of the interferometer without field-widening prisms is characteristic of a conventional interferometer (Fabry-Perot or FTS) operating at the same resolving power, and is given by $\Omega = 2p / R_0$. This limit is defined as the field-of-view at which, for monochromatic light, extreme rays produce one additional fringe across the detector compared with the axial rays. With the field-of-view limited to Ω , a monochromatic interferogram will have highest fringe contrast in the center where all fringe patterns from all angles are in phase, and slightly decreasing contrast towards the edges as the fringes get increasingly out of phase. Due to this phase difference at its edges, the envelope of the interferogram changes from a rectangular function to a rectangle multiplied by a sinc function⁷. The resulting instrumental profile is broadened slightly and resolution is reduced slightly as a result. Further increasing the field-of-view will result in reduced fringe contrast at the ends of the interferogram and an unacceptably broadened instrument function. These considerations are exactly analogous to the trade-off between field-of-view, fringe amplitude, contrast and resolution in Michelson-FTS⁹.

The field of view can be greatly increased through the use of the field widening prisms shown in Figure 1. The fixed prisms serve to rotate the images of the gratings (from a geometrical optics point of view) so that they appear to be normal to the optical axis. In this configuration, the spatial frequency dependence with off-axis angle is minimized for monochromatic light, and fringe patterns with nearly constant contrast across the entire detector are produced even when the field-of-view at the gratings is increased by an order of magnitude above the non-field-widened case. Such a large field-of-view gives SHS an enormous throughput advantage over grating spectrometers that require a narrow slit to achieve high resolving power.

A detailed analysis of field widening shows that the field-of-view of the interferometer is limited by either prism spherical aberration for systems with small Littrow angles, and by prism astigmatism for large Littrow angles¹⁰. For the case of SHIMMER where astigmatism is the limiting factor the maximum field of view can be obtained by using a prism at minimum deviation with angle of incidence η (see Figure 1) given by

$$\frac{(n^2 - 1)}{n^2} \tan h \frac{2n^2 - \sin^2 h}{n^2 - \sin^2 h} = \tan q_L . \quad (4)$$

where n is the prism index of refraction. Once η is determined from Equation 4, the prism apex angle α is given by the condition for minimum deviation through the prism:

$$n \sin\left(\frac{\alpha}{2}\right) = \sin h . \quad (5)$$

The field widening prisms also introduce resolution in addition to the grating dispersion.

The resulting resolving power, R , is given by

$$R = R_0 \left[1 - \frac{\Delta n}{\Delta \lambda} \frac{n}{n^2 - 1} \right] \quad (6)$$

where the correction to R_0 is due to dispersion by the prisms with index of refraction n at wavelength λ .

2.3 Spatial Imaging Considerations

SHS instruments can obtain zero, one or two dimensions of spatial information with appropriate choice of the optics prior to the interferometer. When the scene is imaged by a telescope on the input aperture each point on the interferogram collects light from all points in the scene. In this case the interferogram represents the average spectrum over the field of view of the telescope. However when the scene is imaged on the localization plane of the fringes near the gratings, spatial as well as spectral information can be obtained. If the scene contains only one dimension of spatial information as is the case with SHIMMER (we expect the OH profiles to vary spatially only perpendicular to the earth's limb), an interferogram for each altitude can be obtained by reading out the detector row by row. In situations where intensity variations parallel to the limb distort the interferogram, the spatial information in this dimension can be washed out by using an anamorphic telescope. Two dimensional spatial information along with spectra can be obtained by scanning the field of view during an observation while time tagging detected photons¹¹⁻¹².

3. The SHIMMER Instrument

The SHIMMER instrument has been specifically designed to measure OH solar resonance fluorescence while viewing the limb from low Earth orbit. This measurement is a rigorous test of any hyperspectral imaging technology because retrieval of the OH radiance profile requires highly accurate knowledge of the instrument's performance. In particular, the retrieval of OH spectra from limb observations entails identification and removal of the very bright and spectrally complex ozone-attenuated Rayleigh scattered solar background. This is accomplished by performing a nonlinear least-squares curve

fitting procedure that relies upon very high spectral resolution measurements to properly identify and separate the spectral components of the limb observations. Direct measurements of the moon using a diffuser are used to determine the solar background spectral shape measured by SHIMMER independent of terrestrial OH emission.

The problem is illustrated in Figure 2, where the top panel shows a MAHRSI-measured OH emission spectrum at 70 km tangent height and the underlying Rayleigh scattered solar spectrum. This is the tangent altitude for which OH is most prominent against the Rayleigh scattered solar background. The lower panel shows the OH signal extracted by subtracting the Rayleigh background from the raw spectrum. Since, in effect, the curve fitting algorithm subtracts one large number from another at every wavelength, leaving the residual OH spectrum, any uncharacterized and uncorrected instrumental contributions to the spectral shape will result in large errors in the retrieved OH intensity, particularly for observations of lower tangent heights. The error in the fit of the background shape is greatly reduced by utilizing the full bandwidth of the spectral region of the OH fluorescence. It is the combination of high spectral resolution and extended bandwidth that is essential to the accurate identification of the background spectrum contribution. Further, as the altitude intensity profiles are inverted to yield OH concentration profiles, the intensity errors propagate through the inversion to produce even larger concentration uncertainties. For example, large retrieval and inversion errors will be generated if knowledge of the instrument function and its variation with wavelength or position in the observed scene is incomplete or inaccurate, if the spectral responsivity of the instrument is not well characterized, or if off-axis or internally scattered light is not controlled adequately. The design specifications for the SHIMMER instrument are summarized in Table 1. The spectral resolution, passband, field-of-view, and responsivity requirements of SHIMMER were determined by the previous successful OH measurements by the MAHRSI instrument.

The optical layout is shown schematically in Figure 3. The 500 mm focal length refractive telescope focuses the sky on the gratings. The telescope objective diameter limits the range of angles incident on the gratings while also imaging the scene at infinity on the grating localization plane. This property will be used in SHIMMER to image altitude along the columns of the CCD while producing 1-D interferograms along the rows while limb viewing from space. Telescope aberrations limit the altitude resolution on the limb to 0.87 km. In practice, however, rows will be co-added on the chip to give a 2.2 km (4.3 arc min) altitude resolution.

Out-of-band rejection is achieved by 6.6 cm diameter interference filter between the telescope and interferometer and narrowband multilayer dielectric coatings on the three fold mirrors in the system. All transmitting elements have been AR coated for 308 nm. The interference filter has a 2.3 nm FWHM pass band centered at 308.9 nm. Since the interferometer in this design cannot distinguish between wavelengths at $+\Delta\lambda$ and $-\Delta\lambda$ about the Littrow wavelength, the violet edge of the filter passband is positioned very near the Littrow wavelength (307.0 nm) so that shorter wavelengths are blocked. The interferometer uses an anti-reflection (AR) coated, non-polarizing hexagonal beamsplitter, a pair of 13.02° apex angle field-widening prisms, and a pair of 1200 l/mm, 75% efficiency gratings. For fused silica prisms, 1200 l/mm gratings and a design wavelength of 308.5 nm the Littrow angle of the grating and the optimal angle of refraction of the optical axis leaving the prism are nearly equal (see equations section 2.1), hence the back face of the prisms and the gratings are nearly parallel. For ease of alignment the back prism face and grating face were made parallel for SHIMMER (see table 1). A doublet field lens and a multi-element relay lens focus the plane of the gratings, which is the fringe localization plane, on the CCD. The theoretical modulation transfer function (MTF) of the SHIMMER imaging lenses is shown in Figure 4.

The camera used in SHIMMER utilizes a thinned back-illuminated UV anti-reflection coated CCD manufactured by SITE, Inc with approximately 58% quantum efficiency at 308 nm. The CCD format is 1024 X 1024 with 24 micron square pixels. The camera also includes a shutter mechanism, thermoelectric coolers, cooling fins, and fans for convectively dispelling heat into the cabin air.

The mechanical design for SHIMMER was driven by 5 requirements: 1) locate and support to interferometric precision the optical elements of the interferometer in a manner suitable for Space Shuttle launch and landing loads, 2) locate and fasten the optical components shown in Figure 3 to assure accurate alignment, 3) constrain the mechanical envelope of the instrument to the interior dimensions of the Space Shuttle middeck lockers, 4) provide a simple, robust mating assembly to locate and fasten the instrument to the Space Shuttle crewhatch, and 5) meet all manned-flight program safety requirements.

The interferometric elements, i.e. the beamsplitter, prisms, and gratings, are mounted in a Vascomax steel structure shown in Figure 5 and labeled "interferometer" in Figure 6. The beamsplitter is positioned below the triangular cap visible at the top, and the input and output windows are on the backside. The design allows very precise and stable positioning of the prisms and gratings relative to the beamsplitter. The prism holders are attached to the grating holders, and a spring-loaded turret assembly holds the grating holders tightly to a three-point kinematic mount integral to the cell structure. An interior chamber encloses the CCD Camera and is walled off using light-tight bulkheads and baffle tubes. Both airflow apertures open into this isolated space. Each aperture is covered by a 50 micron mesh screen. The entrance aperture is protected by a transparent Lexan cover that will be removed on-orbit by the flightcrew. The cover plate of the housing unit also provides attach points for lifting handles.

3.1 Operational Considerations

As described above, SHIMMER was designed to conduct a space flight proof-test of the application of the SHS technique to remote sensing of the middle atmosphere. The test will be to observe the vertical profile of OH solar resonance fluorescence by imaging the Earth's sun-illuminated horizon through the UV transmitting optical window in the Space Shuttle Orbiter crewhatch. Tests on three shuttle windows have shown that the panes are not flat enough to cause additional interference effects in SHIMMER interferograms. The instrument is attached to the Orbiter crewhatch using a bracket assembly that utilized a circle of threaded studs located around the optical window. As shown in Figure 7, the bracket includes a hinged channel that supports the instrument and a power converter module. The assembly is hinged to permit folded stowage in a middeck locker.

The crew will maneuver the orbiter to an attitude that will place the SHIMMER line-of-sight tangent to the limb at a nominal altitude of 65 km while placing the window out of the sun's direct illumination. The projected 2.3 degree instrument field of view will then have an upper boundary at 100 km altitude and a lower boundary at 30 km altitude. At a wavelength of 308nm, the vertical radiance profile of Rayleigh scattered sunlight has a well-defined maximum at about 41 km altitude. The flight crew will confirm the pointing of the instrument by observing the placement of this radiance peak in the field-of-view displayed on a laptop computer. The crew then will initiate several sequences of nominal (1.2 sec) exposures. The data will be downlinked in near real-time to an operations control center at Johnson Space Center where the SHIMMER science team will analyze the data and provide feedback to the crew. After the flight the data will be analyzed to produce OH number density profiles using algorithms validated in the laboratory and on MAHRSI data.

4. Instrument Characterization in the Lab

An extensive series of laboratory tests has verified that SHIMMER has met design expectations. The most basic test is to observe the interferogram produced by a monochromatic source within the instrument's spectral filter passband ($\%T > 35\%$ from 307.8 nm to 309.6 nm). A Zn pen-ray lamp with a single bright emission at 307.6 nm was used for optimization and testing. The spectral width of the emission is not resolved by the interferometer. The fringe pattern recorded by SHIMMER using the Zn pen-ray source is shown in Figure 8. Note that all spectral information is in the horizontal dimension, and the vertical dimension is exclusively an image of the vertical intensity distribution of the source. When applied to the OH limb-viewing problem, the vertical dimension will be aligned perpendicular to the limb so that each row of the CCD will record the spectrum observed at distinct viewing angles corresponding to distinct tangent heights.

As discussed in section 2.1, grating figure errors and interferometer refractive index inhomogeneities distort the Fizeau fringe pattern recorded at the CCD, but with the high quality optics of SHIMMER, these distortions are negligible. The interferogram was corrected for dark field and nonuniformity, then Fourier transformed to produce the spectrum shown in Figure 9. Since the Zn line at 307.6nm is unresolved by the instrument, this spectrum represents the achieved instrument function.

The passband of the instrument is determined by the spectral filter, the spectral resolution, the number of pixels sampling the interferogram, and the image quality at the CCD. In these tests, the image of the gratings is focused onto 1024 pixels, so the number of spectral elements available without aliasing is 512. The maximum passband assuming perfect imaging should be 512 times the spectral resolution (0.0058 nm as verified using OH emission as described below), or about 3.0 nm.

Tests with a polychromatic source were conducted with a microwave excited OH lamp. These tests verified that the spectral resolution, bandwidth, and field-of-view all meet design specifications. With the gratings adjusted for a Littrow wavelength of 306.42 nm, the OH spectrum shown in the first panel of Figure 10 was recorded. The spectrum in the second panel was generated using OH g-factors assuming a solar source and a rotational temperature of 2000 K. The figures show that the two features at 307.526 nm and 308.607 nm are recorded in spectral resolution elements 213 and 395. This coupled with the one pixel wide line shape in the Zn spectrum in Figure 9 verify a spectral resolution of 0.0059 nm, or a resolving power of 53500 as designed. The second panel shows the OH spectrum and filter transmission folded about the Littrow wavelength of 306.42 nm. As mentioned above, the interferometer cannot distinguish between wavelengths at $+\Delta\lambda$ and $-\Delta\lambda$ about the Littrow wavelength, but since the short wavelength edge of the filter passband is very near the Littrow wavelength, the wavelengths to the violet of Littrow are blocked.

The average spectral responsivity of the instrument has been measured using a calibrated Labsphere, Inc. integrating sphere with an 8" diameter aperture, internal Spectralon diffuse reflecting tiles, and multiple halogen lamp sources. The absolute spectral radiance of the sphere was measured at the NASA/Goddard Space flight Center Laboratory for Atmospheres in collaboration with the SSBUV group¹³⁻¹⁴. The SHIMMER field-of-view footprint is within the sphere's aperture. The total signal at the CCD (digital numbers, DN) is related to the total inband photon flux at the SHIMMER input aperture by

$$S(\text{DN}) = f(\text{phot/sec}) \times t_{\text{int}}(\text{sec}) \times \bar{T}_{\text{filt}} \times \bar{T}_{\text{opt}} \times \text{QE}_{\text{CCD}} (e^-/\text{phot}) \times G(\text{DN}/e^-), \quad (7)$$

where t_{int} is the exposure time, \bar{T}_{filt} and \bar{T}_{opt} are the average spectral filter and optical element transmission over the passband of the instrument, and QE_{CCD} and G are the

quantum efficiency and gain of the CCD. The total inband photon flux, ϕ , is related to the spectral radiance of the integrating sphere, L_γ (in kiloRaylieghs per nm), by

$$f(\text{phot/sec}) = L_\gamma (\text{kR/nm}) \times \frac{10^9}{4\pi} \times \Delta\lambda(\text{nm}) \times A(\text{cm}^2) \times \Omega(\text{sr}), \quad (8)$$

where $\Delta\lambda$ is the bandwidth, A is the input aperture area, and Ω is the field-of-view. The measured responsivity of SHIMMER is $R=4.34 \times 10^4 \text{ DN sec}^{-1} \text{ kR}^{-1}$, the derived optical transmission is $\bar{T}_{\text{opt}} = 0.18$, and the calculated throughput is $\bar{T}_{\text{opt}} \bar{T}_{\text{filt}} A \Omega = 4.5 \times 10^{-3}$, all meeting instrument design goals.

5. SHIMMER Earth-Limb Measurement Simulation

Model interferograms have been generated in order to predict the performance of the instrument while viewing the limb from space. High-resolution OH g factors, solar spectrum, and spectral filter contributions are combined to produce an effective incident spectrum. The CCD rows representing a 1.2 sec integration have been binned into 32 row slices to increase the signal-to-noise ratio, with the OH and solar contributions appropriately weighted based on MAHRSI measurements of OH and Rayleigh scattered background intensity collected during the STS-85 shuttle mission. Assuming a unit power image of the gratings at the CCD, the digital numbers per pixel per slice

$$S_{\text{CCD}}(i, j) = \int_{y(j)}^{y(j+1)} \int_{x(i)}^{x(i+1)} \int_0^\infty L_{\text{OH}}(\mathbf{s}, y) R(\mathbf{s}) \{1 + \cos[2\mathbf{p}(4(\mathbf{s} - \mathbf{s}_0)x \tan \mathbf{q})]\} d\mathbf{s} dx dy \\ + \int_{y(j)}^{y(j+1)} \int_{x(i)}^{x(i+1)} \int_0^\infty L_{\text{sun}}(\mathbf{s}, y) R(\mathbf{s}) \{1 + \cos[2\mathbf{p}(4(\mathbf{s} - \mathbf{s}_0)x \tan \mathbf{q})]\} d\mathbf{s} dx dy \quad \text{DN/pixel/slice} \quad (7)$$

(DN/pixel-slice) due to altitude-dependent spectral radiances L_{OH} and L_{sun} (kR) is calculated using the equation,

where i is the CCD pixel number along rows, j is the slice number corresponding to one of 32 tangent height altitudes in the range 30 - 94 km, $x(i)$ and $y(j)$ is the location on the grating imaged onto the corner of CCD region (i,j) , and the responsivity, $R(\sigma)$, which incorporates entrance aperture size, pixel field-of-view, optical transmission, CCD quantum efficiency, integration time, and A/D converter gain converts radiance at the limb (kR) to signal readout from the CCD camera (DN/pixel/slice). Figure 11 shows the interferogram produced by anticipated OH emissions and Rayleigh scattered sunlight. The emissions from lower altitudes, about a factor of 40 brighter than those from higher altitudes, are imaged at the bottom of the CCD. The line at zero optical path difference, at which the frequency components due to all wavelengths and incidence angles are in phase, is evident in the central column. The upper panel shows the signal (solid lines) and noise (dashed lines) components present in the interferogram at the CCD due to atmospheric emissions and instrumental effects. All the curves shown in the upper panel have units DN/pixel/slice. These curves indicate the relative contribution to the interferogram as a function of altitude for each of the signal and noise sources. Notice that the total signal and noise are dominated by Rayleigh scattered background at all altitudes. Note also that instrumental noise contributions are only significant above about 85 km, and that the total noise becomes comparable to or dominates OH signal only above 85 km and below 40 km.

Estimates of the signal-to-noise ratio at each altitude were made by 'retrieving' OH intensity as a function of altitude from the interferogram in the same way as will be done during the mission. The procedure entails subtracting darkfield, flat fielding, calibration to radiance units, Fourier transforming, phase correction, nonlinear curvefitting to remove Rayleigh scattered background, and integration over OH features. The bottom panel shows the retrieved OH spectral features (horizontal) as a function of altitude (vertical). The retrieved radiance as a function of altitude (shown in Figure 12) is the

same as the radiance profile input to the instrument model in the first place, as it should be. The estimated precision of the measurement as a function of altitude (shown in Figure 13) is determined not only by the signal-to-noise ratio in the interferogram, but also by the bandwidth and spectral shape of the incident spectrum.

6. Future Developments

We are currently pursuing further miniaturization of an OH SHS with the support of NASA's Planetary Instrument Definition and Development Program (OSS PIDDP). Further reduction in instrument size and weight will be achieved by optically contacting the interferometer components to form a monolithic interferometer. This technique makes the complex Vascomax structure, which is used in SHIMMER to hold the optical components in precise proximity, obsolete. Furthermore the alignment of a monolithic interferometer is virtually impervious to vibrations, resulting in a major risk reduction for space flight applications. Figure 14 shows a photograph of the monolithic instrument presently under construction. It will have 200 times the throughput of MAHRSI and a spectral resolution of 0.012nm. We plan to report on the performance of the monolithic instrument in the near future.

The latest achievements in spatial heterodyne spectroscopy and the ongoing work confirm that this technique is remarkably well suited for the investigation of planetary atmospheres from space. For example, long standing issues like the polar mesospheric cloud phenomenon on Earth or the detailed understanding of the photochemistry in the Martian atmosphere can be addressed using global [OH], [NO] and/or temperatures provided by high spectral resolution UV limb spectra acquired from an orbiting platform.

Acknowledgements

The authors would like to acknowledge Mike Stevens and Charles Brown at the Naval Research Laboratory, and Lee Potratz at the University of Wisconsin-Madison for his

assistance in fabrication SHIMMER. This work is supported by grants ATM-9612228 from the National Science Foundation, the Planetary Instruments Definition and Development Program of NASA's Office of Space Science and the Air Force Space Test program. Part of this work was performed while C.E. held a National Research Council - NRL Research Associateship.

References:

1. D.R. Bates and M Nicolet, "The photochemistry of atmospheric water vapor", J. Geophys. Res., **55**, 301-327 (1950).
2. M. E. Summers, R.R. Conway, D.E. Siskind, D. Offermann, P. Preusse, J.M. Russel, "Implications of Satellite OH Observations for Middle Atmospheric H₂O and Ozone", Science, **277**, 1967-1970 (1997).
3. R. R. Conway, M.E. Summers, M.H. Stevens, J.G. Cardon, P. Preusse, D. Offermann, "Satellite Observations of Upper Stratospheric and Mesospheric OH: The HOx Dilemma", Geophys. Res. Lett., **17**, 2613-2626 (2000).
4. M.E. Summers and R.R. Conway, "Insights into middle atmospheric hydrogen chemistry from analysis of MAHRSI OH observations", Geophysical Monograph 123, 117-130 (2000).
5. G. E. Thomas, "Mesospheric clouds and the physics of the mesopause region", Rev. Geophys., **29** 553-575 (1991).
6. R. R. Conway, M.H. Stevens, C.M. Brown, J.G. Cardon, S.E. Zasadil, G.H. Mount, "The Middle Atmosphere High Resolution Spectrograph Investigations", J. Geophys. Res., **104**, 16,327-16,348 (1999).
7. J. Harlander, "Spatial Heterodyne Spectroscopy, interferometric performance at any wavelength without scanning", Ph.D. Thesis, University of Wisconsin-Madison, (1991).

8. J. Harlander, R.J. Reynolds, F.L. Roesler, "Spatial Heterodyne Spectroscopy for the exploration of diffuse interstellar emission lines at far ultraviolet wavelengths", *Ap.J.*, **396**, 730-740 (1992).
9. J.W. Brault, "Fourier transform spectroscopy". In A. Benz, M. Huber, & M. Mayor (Eds.), *High Resolution in astronomy: Fifteenth Advanced Course of the Swiss Society of Astronomy and Astrophysics* (pp. 1-61). Sauverny, Switzerland: Geneva Observatory. (1985).
10. J.M. Harlander and F.L. Roesler. "Spatial Heterodyne Spectroscopy" in preparation 2001.
11. J.M. Harlander, H.T. Tran, F.L.Roesler, K.P.Jaehnig, S.M.Seo, W.T.Sanders, and R.J. Reynolds. "Field-Widened Spatial Heterodyne Spectroscopy: Correcting for Optical Defects and New Vacuum Ultraviolet Performance Tests" in *EUV, X-Ray and Gamma-Ray Instrumentation of Astronomy V*, SPIE meeting proceedings, **2280**, 310-319. (1994).
12. Barham W Smith and John M Harlander,., "Imaging spatial heterodyne spectroscopy: theory and practice". in *Infrared Technology and Applications XXV*, Bjorn F. Andresen; Marija Strojnik Scholl; Eds. Proc. SPIE Vol. **3698**, 925-931 (1999).
13. E. Hilsenrath, D.E. Williams, R.T. Caffrey, R.P. Cebula, S.J. Hynes, "Calibration and radiometric stability of the Shuttle Solar Backscatter Ultraviolet (SSBUV) experiment." *Metrologia*, **30:(4)**, 243-248 (1993).
14. S. Janz, E. Hilsenrath, J. Butler, D.F. Heath, R.P. Cebula, "Uncertainties in radiance calibrations of backscatter ultraviolet (BUV) instruments". *Metrologia*, **32:(6)**, 637-641, (1996).

Table I SHIMMER Design Specifications

System	Interference filter	2.3 nm FWHM centered at 308.9 nm 307.0 nm - 310.5 nm full width
	Entrance optics Exit optics Detector	500 mm fl telescope 7 element relay system 1024 X 1024 24 μ m CCD
	Gratings Clear aperture Groove density Littrow angle Littrow wavelength	20 x 20 mm 1200 l/mm 10.7° 307.0 nm
	Field-widening prisms Clear aperture Wedge angle Incident angle Exit angle	22 x 22 mm 13.02° 8.73° 10.7°
	Beamsplitter Clear aperture	28 x 28 mm
	Field of view At gratings On sky	10° 2.3 x 2.3°
Performance	Resolving power	53,500
	Spectral resolution	0.0058 nm
	Non-aliased spectral range	2.95 nm
	Achieved spectral range	Filter limited
Resources	Sky imaging	1.7 arc min
	Mass	22 Kg
	Volume	52 x 42 x 23 cm ³
	Power	27 W
	CCD Readout	72kB / 8 sec
	Image Rate	375 images / orbit
	Data Rate	27 Mbytes / orbit

Figure 1. Conceptual diagram of a field-widened SHS.

Figure 2. MAHRSI detection of OH at 70km tangent height.

Figure 3. SHIMMER block diagram and optical layout.

Figure 4. Theoretical Exit Optics MTF. The three solid curves are for on axis, 70% field and full field points on the gratings. The dashed curve shows the diffraction limited MTF. The pixels on the CCD limit the maximum frequency to 21 cycles/mm.

Figure 5. SHIMMER components on the flight baseplate in the laboratory.

Figure 6. SHIMMER component layout.

Figure 7. SHIMMER Bracket assembly

Figure 8. Interferogram recorded in the laboratory

Figure 9. Measured Zn emission feature at 307.6 nm

Figure 10. OH spectrum measured in the lab compared with theoretical OH spectrum

Figure 11. Modeled signal and noise contributions (top), 1024 X 32 pixel interferogram (middle), and 512 X 32 spectral resolution element retrieved OH (bottom).

Figure 12. Modeled OH altitude intensity profile.

Figure 13. Estimated OH radiance measurement precision.

Figure 14. Full-scale model of a miniature monolithic version of SHIMMER.

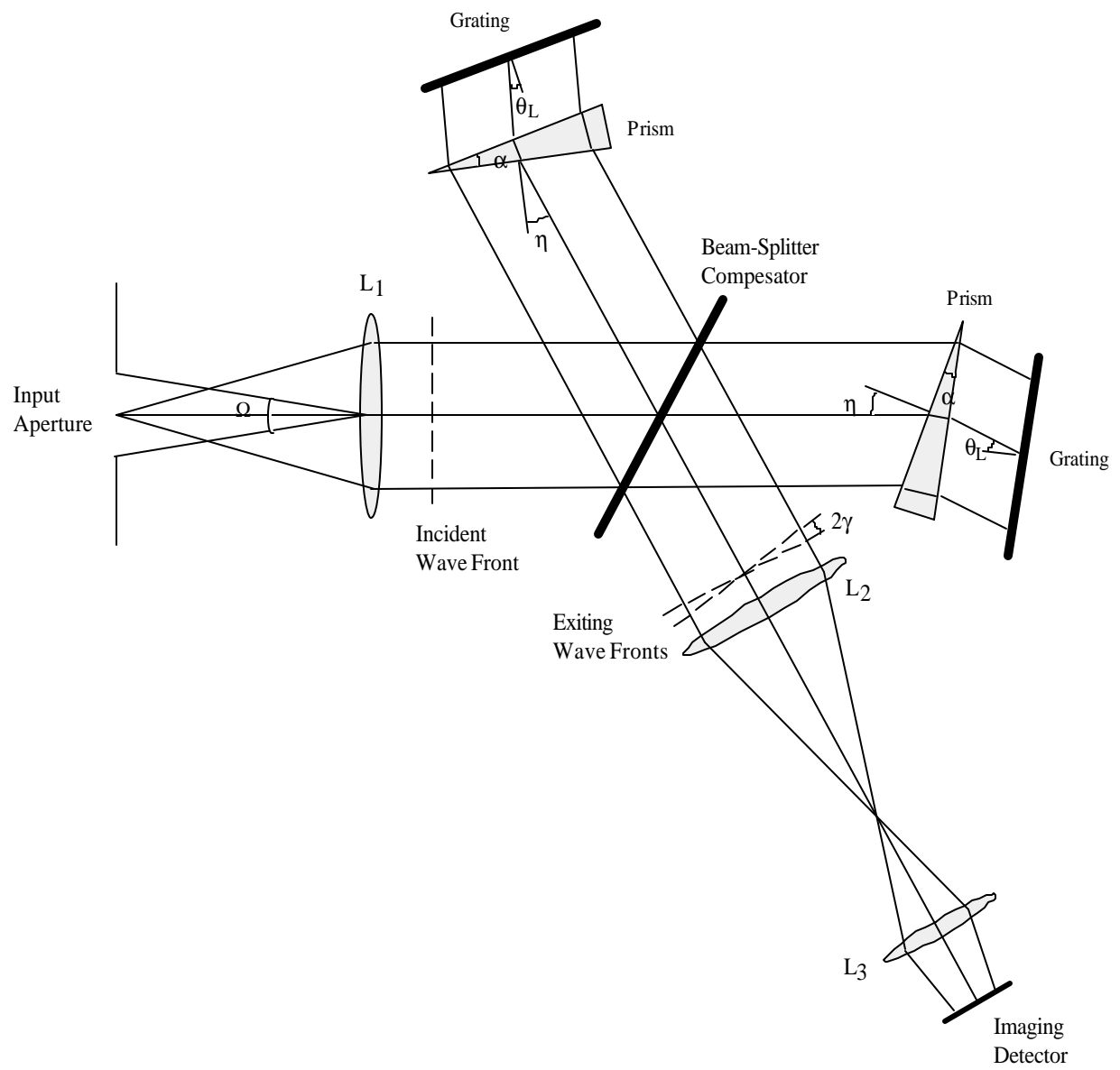


Figure 1

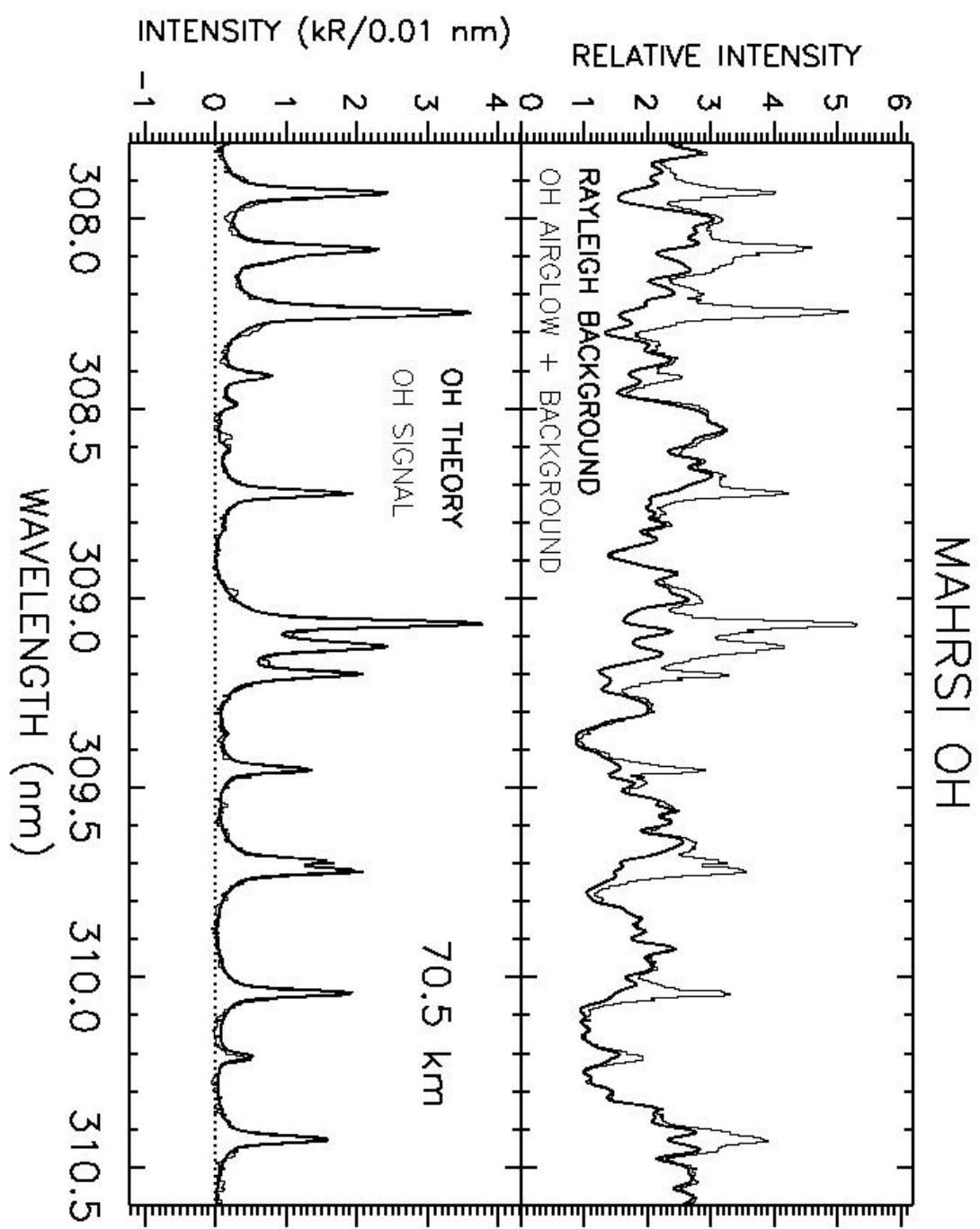


Figure 2.

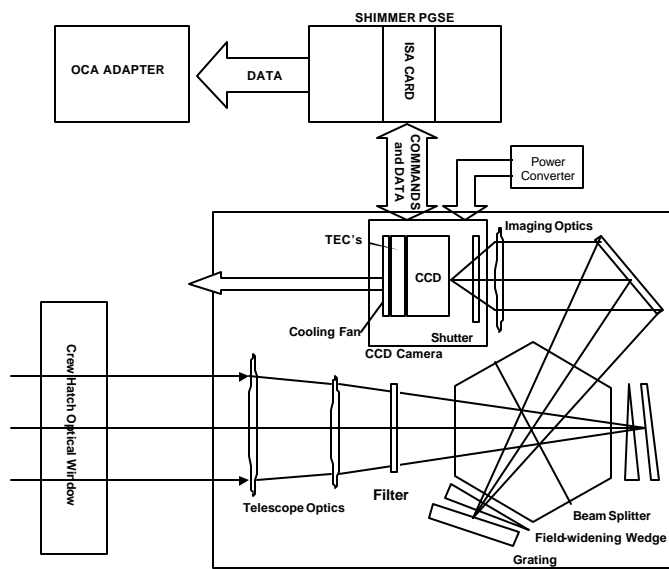


Figure 3.

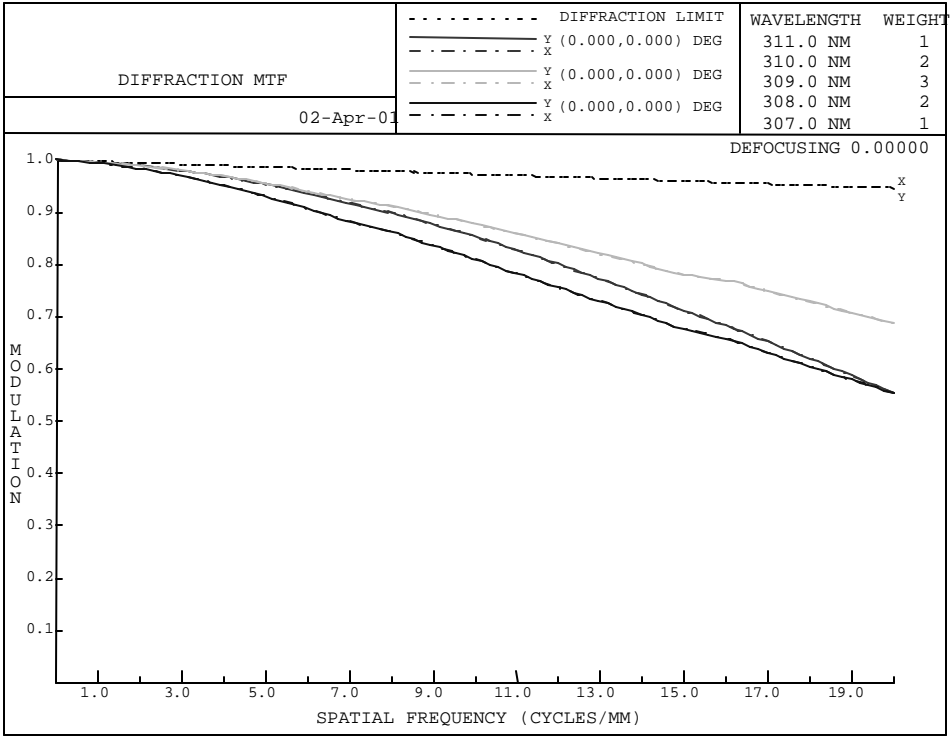


Figure 4.



Figure 5.

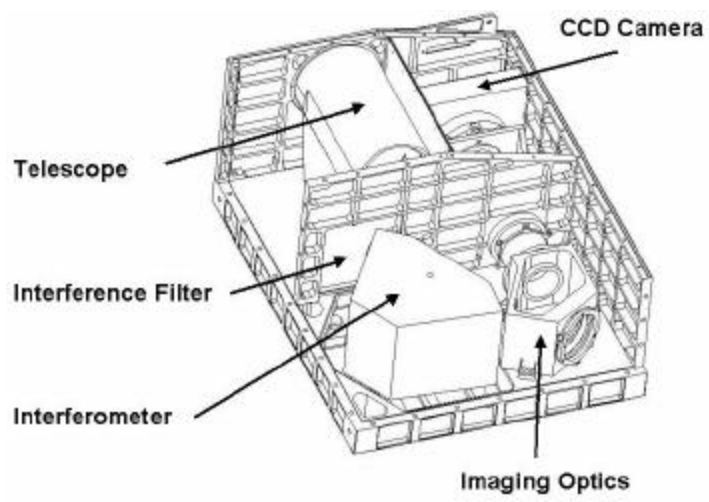


Figure 6.

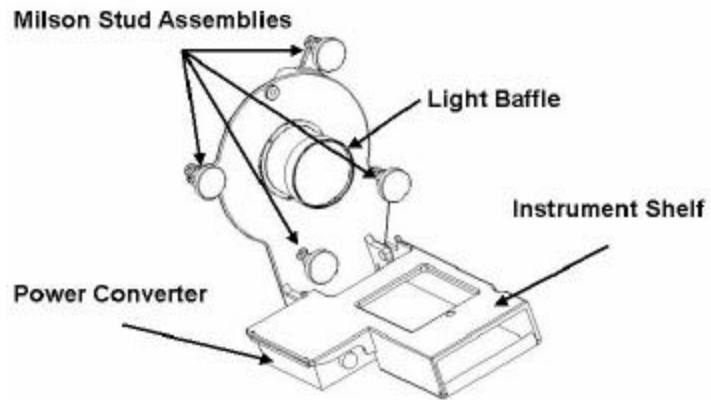


Figure 7.

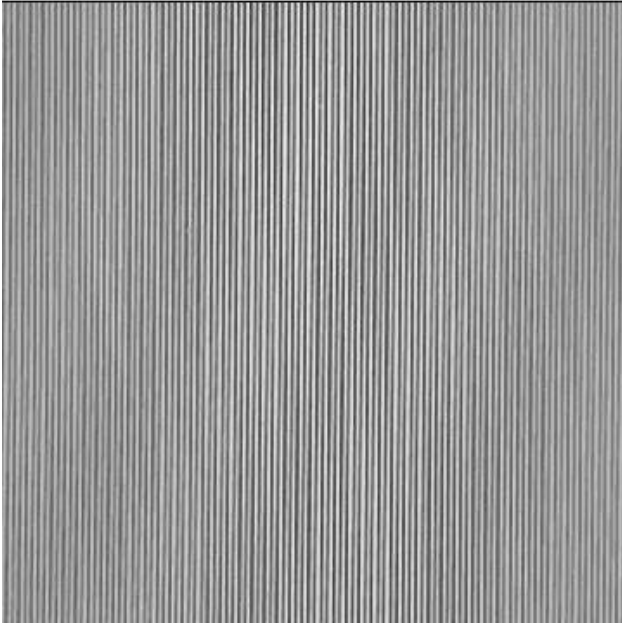


Figure 8.

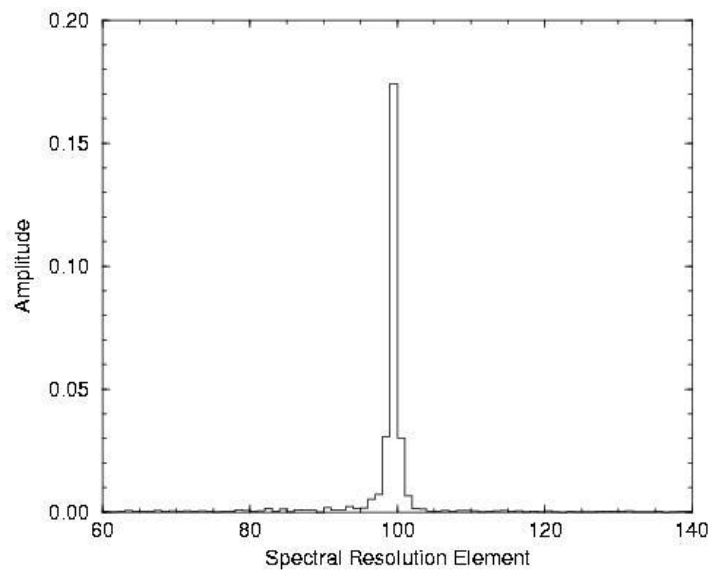


Figure 9.

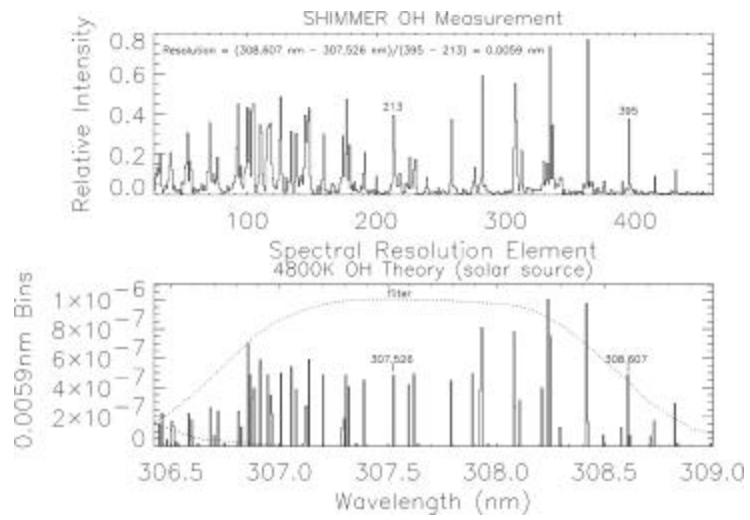


Figure 10.

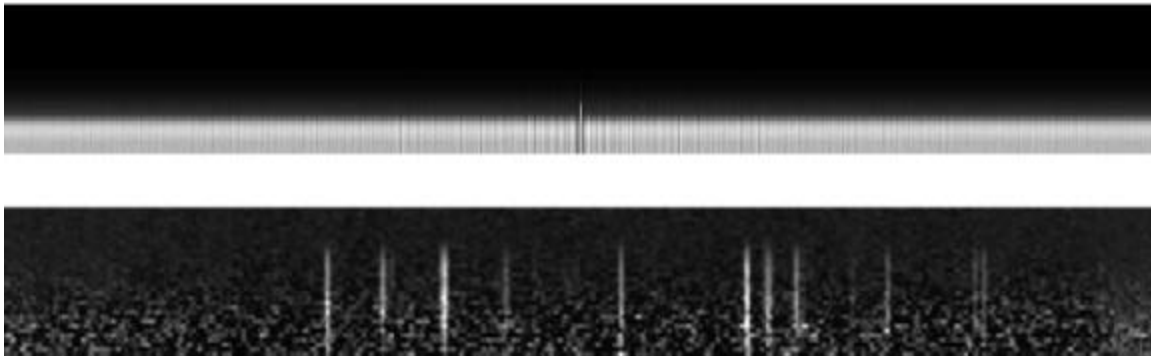
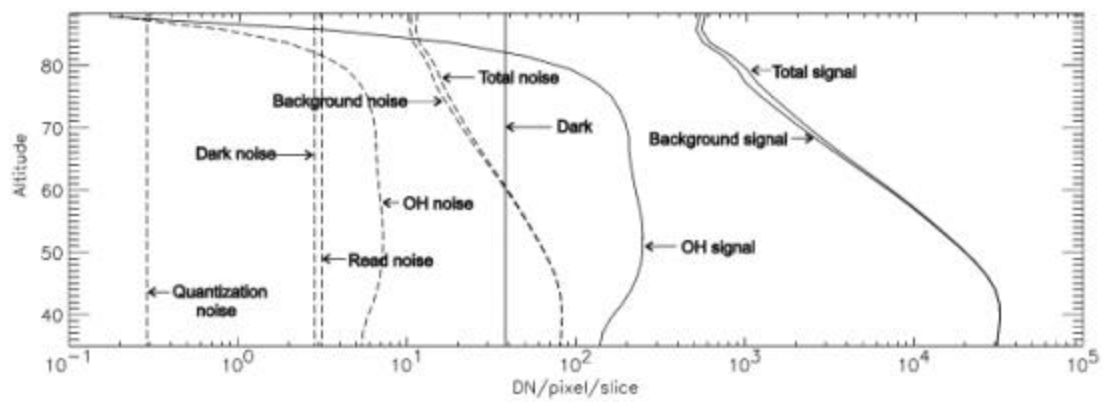


Figure 11.

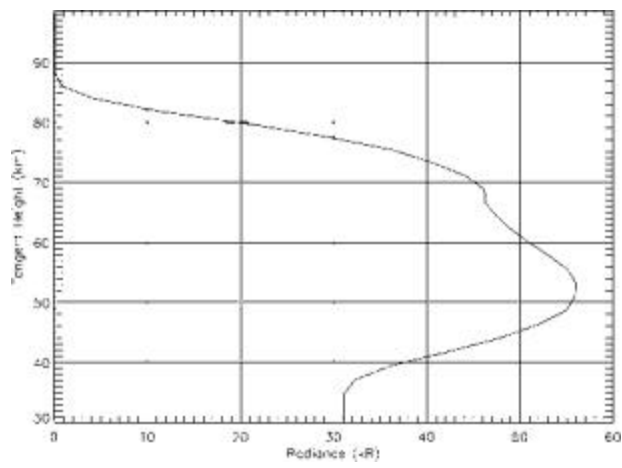


Figure 12.

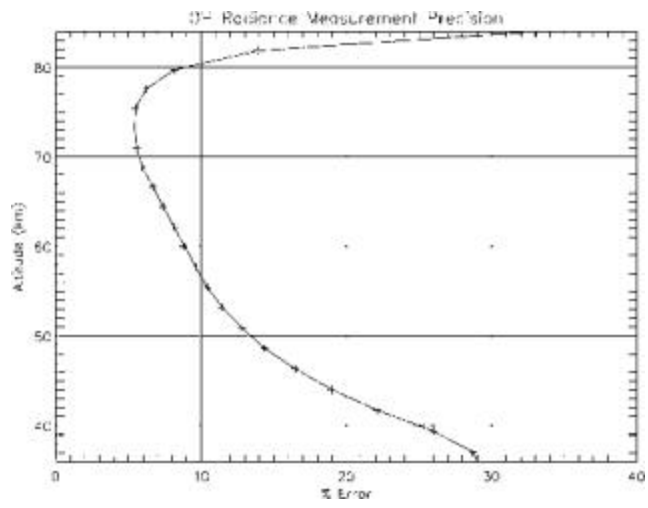


Figure 13.

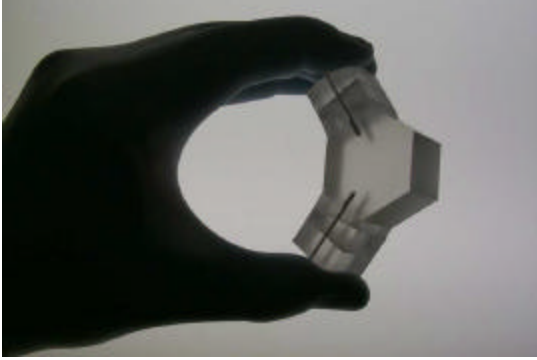


Figure 14.